Research Square

Preprints are preliminary reports that have not undergone peer review.
They should not be considered conclusive, used to inform clinical practice,
or referenced by the media as validated information.

Tailoring pore architecture and residual carbon ordering in vat-photopolymerized SiC ceramics via debinding temperature

Zhiwei Wang
Shanghai Institute of Technology
Shijie Xu
Shanghai Institute of Technology
Li Yang
Shanghai Institute of Technology
Xiaomin He
Jiaxing CeramPlus Technology Co., Ltd
Jindan Tian
Shanghai Institute of Technology
Yanlin Jiang
Jiaxing CeramPlus Technology Co., Ltd
Bohang Xing
Shanghai Institute of Technology
Paul Bowen
Jiaxing CeramPlus Technology Co., Ltd
Zhe Zhao
zhezhao@sit.edu.cn

Shanghai Institute of Technology

Research Article

Keywords: Porous SiC ceramic, Pore architecture, Mercury intrusion porosimetry, Vat photopolymerization, Debinding, Residual carbon

Posted Date: November 18th, 2026

DOI: https://doi.org/10.21203/rs.3.rs-11424871/v1

License: This work is licensed under a Creative Commons Attribution 4.0 International License.
Read Full License

Additional Declarations: No competing interests reported.

Tailoring pore architecture and residual carbon ordering in vat-photopolymerized SiC ceramics via debinding temperature

Zhiwei Wang [a], Shijie Xu [a], Li Yang [a], Xiaomin He [b], Jindan Tian [a], Yanlin Jiang [b], Bohang Xing [a], Paul Bowen[b], Zhe Zhao [a,b,*]

[a] School of Material Science and Engineering, Shanghai Institute of Technology, Shanghai 201418, China

[b] Jiaxing CeramPlus Technology Co., Ltd., Jiaxing 314100, China

*Corresponding author. zhezhao@sit.edu.cn (Z. Zhao)

Abstract: Vat photopolymerization (VPP) of SiC ceramics produces green bodies that contain about 45 vol% organic phase, so thermal debinding does not simply remove a fugitive binder but defines the pore architecture on which both the subsequent solid-state sintering and the pore-related functionality depend. This work examines how the debinding temperature (450–650 °C) governs the open pore structure, the structural ordering of the residual carbon and the porosity–strength relationship of pressureless-sintered SiC ceramics. Mercury intrusion porosimetry shows that the open porosity rises from 27.25% at 450 °C to a maximum of 35.92% at 600 °C, with a single pore-size peak between 100 and 300 nm, while the total pore area falls from 9.07 to 2.67 $m^2 g^{-1}$, indicating that a tortuous, high-surface-area pore network is replaced by a coarser and better-connected one. EDS and Raman spectroscopy show that the residual carbon is progressively enriched and reaches its highest structural order at 600 °C (ID/IG = 0.63). The ceramic debound at 600 °C combines a sintered porosity of 13.99%, a density of 2.77 g cm^{-3} and a flexural strength of 290.2 ± 24.3 MPa, and the strength–porosity data follow the Ryshkewitch–Duckworth relation (σ_0 = 394.9 MPa, b = 2.36, R^2 = 0.949). The debinding temperature therefore provides a single processing lever for the design of porous VPP-SiC components with a controlled open pore fraction and load-bearing capacity.

Keywords: Porous SiC ceramic; Pore architecture; Mercury intrusion porosimetry; Vat photopolymerization; Debinding; Residual carbon

1 Introduction

Silicon carbide (SiC) ceramic possesses outstanding high-temperature mechanical strength, excellent thermal shock resistance, superior chemical corrosion stability and good oxidation resistance[1]. These properties make it one of the most promising structural ceramic materials for high-temperature industrial furnaces, aerospace thermal protection systems, nuclear reactor core components and extreme-condition corrosion-resistant service parts [2, 3]. Compared with conventional dry pressing, slip casting [4]

and hot pressing forming technologies [5], photopolymerization additive manufacturing can effectively remove the oxide layers on silicon carbide surfaces and improve the final mechanical properties [6]. It enables the fabrication of complex-shaped SiC ceramic components with high dimensional accuracy and fine surface quality, which effectively breaks through the shape limitation of traditional ceramic forming methods and broadens the engineering application scenarios of high-performance SiC structural ceramics[7].

Nevertheless, the photopolymerized SiC ceramic green body contains a large amount of photosensitive resin monomers, dispersants, and photoinitiators [8]. The thermal debinding process for removing organic phases is therefore an essential and prerequisite procedure before high-temperature sintering, which directly determines the microstructure homogeneity and the final sintering densification of SiC ceramics. An inadequate debinding process can often lead to issues like sample cracking [9]. Therefore, the development of a well-established debinding protocol is crucial for the successful sintering of samples. Typically, the debinding protocol requires testing the thermal weight-loss curve of the green bodies for formulation**.** The thermal debinding temperature is the core technological parameter dominating the pyrolysis behavior of organic components and the residual carbon evolution characteristics of photopolymerization SiC green bodies [10]. During the inert atmosphere debinding process, the organic binder undergoes continuous thermal decomposition, chain scission and carbonization reactions, and the residual carbon generated by incomplete pyrolysis cannot be completely removed under nitrogen protection conditions [11, 12]. This residual carbon remains inside the green body and evolving into different carbon forms including amorphous disordered carbon and ordered graphite-like carbon [11, 12]. Existing studies have mostly focused on the influence of sintering aid content and sintering temperature on the densification behavior and mechanical properties of SiC ceramics [13], while less attention has been paid to the inherent correlation between debinding process parameters, residual carbon content, carbon morphology and spatial distribution[14]. In particular, the microscopic regulation mechanism of residual carbon segregation and structural evolution induced by excessive debinding temperature on pore aggregation, grain growth heterogeneity and lattice distortion of sintered SiC ceramics still lacks systematic and in-depth clarification[15].

Rather than an unavoidable deficiency, the porosity inherited from debinding is the structural feature through which VPP SiC is converted into a porous material with a designed architecture. The green body contains approximately half of photosensitive

resin; the removal of this organic phase during debinding generates an interconnected pore network inside the sample [16]. Because the solid loading of the photocurable slurry is limited to about 55 vol% by its viscosity and curing behaviour, this network cannot be closed by pressureless solid-state sintering at 2150 °C: SiC is strongly covalent and its atomic diffusion rate is low, so mass transport between grains fills only part of the pore space inherited from debinding. The residual carbon that remains between the SiC particles after debinding occupies a further part of it. The open pore fraction, the pore-size distribution and the connectivity of the network are therefore determined by the debinding schedule and are retained, in a modified form, in the sintered body. This offers a route to porous SiC components whose porosity and pore morphology are set at the green-body stage and whose strength follows from that architecture, which is the property combination required for filters, supports and other pore-function-dominated applications.

It should be noted, however, that the residual carbon formed during debinding is not merely a detrimental byproduct. For instance, the residual pyrolytic carbon has been observed to form a network structure connecting SiC particles [16]. Wang et al. have demonstrated that the residual carbon is a key sintering additive for achieving high-performance, dense SiC ceramics through solid-state sintering[17]. A lower degree of defects in the residual carbon has been shown to promote grain growth and reduce neck size during pressureless sintering [17]. Accordingly, the characteristics of residual carbon can be precisely tailored by regulating the debinding procedure, thereby optimizing grain growth and interfacial bonding during the solid-state sintering of SiC ceramics[18, 19]. The major weight loss occurs between 300 °C and 600 °C, where the photopolymerized resin backbone undergoes thermal decomposition, chain scission, and carbonization[20, 21]**.** Above 600 °C, debinding is essentially complete, but this residual carbon remains, playing a decisive role in the solid-state sintering process[22, 23]. Therefore, optimizing the debinding process is essential for achieving a homogeneous, high-quality microstructure[24].

In this work, photopolymerization additive manufacturing combined with solid-state sintering was used to fabricate high-performance SiC structural ceramics. Focusing on the core problem of residual carbon evolution induced by different debinding temperatures, the intrinsic relationship between debinding process parameters, residual carbon content and structural characteristics, pore structure evolution and sintering densification behavior was systematically explored. The microstructure morphology, pore structure parameters, residual carbon structural order and grain boundary phase

distribution of SiC ceramics prepared at different debinding temperatures were characterized by SEM, mercury intrusion porosimetry, Raman spectroscopy, EDS and EBSD(Electron Backscatter Diffraction). In particular, EPMA (Electron Probe Microanalysis) for carbon characterization can only be applied to sintered ceramics, and is not applicable to ceramic green bodies. The synergistic regulation mechanism of ordered residual carbon and B_4C sintering aid on optimizing grain boundary structure and inhibiting pore aggregation was clarified. The microstructural deterioration mechanism of residual carbon segregation and disorder evolution caused by excessive debinding temperature on ceramic densification was revealed. The aim is to provide a reliable theoretical basis and process reference for the controllable preparation of uniform-microstructure and high-performance photopolymerization SiC ceramics by optimizing thermal debinding technology. The pore architecture of the debound green bodies and of the sintered ceramics is therefore treated here as the central design target , and the porosity–strength relation is used to define the processing window within which the open pore fraction can be varied without loss of load-bearing capacity.

2. Materials and methods

2.1 Materials

Commercial resin, dispersant, photoinitiator, SiC powder, commercial Digital Light Processing (DLP) advanced additive manufacturing equipment, vacuum mixer, ultrasonic instrument, and other equipment used in this study were provided by Jiaxing CeramPlus Technology Co., Ltd. Table 1 lists all chemicals to prepare a mixture of the photosensitive resin as the printable SiC photocurable slurry. All chemicals were obtained from a commercial supplier and used directly in this work without further modification.

Table 1 Composition of the optimized photosensitive resin

Composition		Type
Resin	NPGDA	Bifunctional acrylate monomer
	TPMETA	Trifunctional acrylate monomer
	TMP3EOTA	Trifunctional acrylate monomer
	HEMAP	Trifunctional acrylate monomer
Photoinitiator	CPI05	Free radical photoinitiator
	CPI06	Free radical photoinitiator

Dispersant	CPD07	/
α-SiC	CP-SC-07	dv50 = 10.5μm, purity ≥ 99.3%
	CP-SC-12	dv50 = 1 μm, purity ≥ 99.3%
B_4C	CP-BC-08	dv50 = 0.6μm, purity ≥ 99%

Note: a: The amount of photoinitiator added was based on the total resin weight.

b: The amount of dispersant added was based on the total powder weight.

2.2 Preparation of green bodies

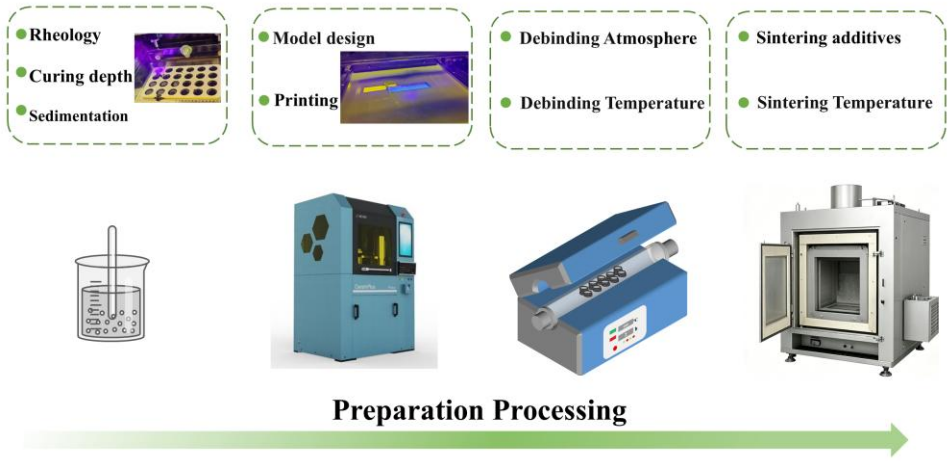


Figure 1. Flow diagram of the preparation of SiC Ceramic by VPP

As shown in Figure 1, the complete fabrication process includes slurry preparation, SiC sample printing, green body debinding, and SiC sintering. For the slurry system, the most critical parameters are rheological behavior, curing depth, and sedimentation. Since sedimentation has been systematically investigated in our previous studies and was found to be negligible under the current conditions, it will not be further discussed in this work. With regard to the printing process, both model design and parameter settings significantly influence printing quality. During the debinding stage, the atmosphere and temperature critically affect microcrack formation in the samples. Although the influence of debinding atmosphere on SiC ceramics has been thoroughly examined in our prior work [17], this study focuses specifically on the effects of debinding temperature. As for the sintering process, within the same temperature range, sintering additives demonstrate a remarkable influence on the densification degree of samples. First, the resin monomer, photoinitiator, and dispersant were added to a beaker according to the proportions shown in Table 1. The resin was then poured from the

beaker into a slurry tank(55vol%). Next, coarse and fine SiC powder with 60wt.% and 40wt.% was mixed with B_4C in the slurry tank. The mixed powder was combined with the photosensitive resin was then poured into a vacuum-degassing mixer. The mixture was stirred at a speed of 1500 rpm for 5 minutes to remove air bubbles, resulting in the 55vol% SiC slurry. Finally, the SiC slurry was poured into the material tank of a commercial Digital Light Processing (DLP) advanced manufacturing equipment (Jiaxing CeramPlus Technology Co., Ltd. RJ-HID -385). After importing the printing model, the SiC green body was printed using the exposure parameters shown in Table 2. According to Table 3 gives the details of the debinding, the green body was heated to 450-650℃ in a tube furnace and kept for 4 hours for debinding in Nitrogen(99%). The weight loss during debinding was measured using an analytical balance, and the green body mass was recorded before and after the thermal treatment to determine the residual carbon content. Finally, the samples were passed to a pressureless sintering furnace and sintered at 2150°C for 2 hours, and then naturally cooled.

2.3 Characterization Methods

The curing thickness is the thickness of a single cured layer of each specimen. The ceramic microstructures were observed using the Phenom Pro scanning electron microscope (SEM) from Phenom-World B.V. (Shanghai). As shown in Figure 2, the rheological properties of the slurry were tested using the Kinexus pro rotational rheometer manufactured by Malvern Instruments Ltd. (UK). The slurry underwent single-layer ultraviolet curing (λ=385nm, light intensity: 200mW/cm²) using an LED light source produced by Shenzhen Shanglin Technology Co., Ltd. The dimensions of green bodies were measured using a Vernier caliper (model 111N-102-40) produced by Guanglu Digital Measuring Instrument Co., Ltd. The density of the sintered samples was determined by the Archimedes method with an analytical balance. The three-point bending strength of the SiC ceramic was tested on the SUN500-type universal material testing machine provided by Jiaxing CeramPlus Technology Co., Ltd. The specimen size was 3×4×35mm, with a span of 30mm, and a loading rate of 0.5mm/min. Phase identification was performed through X-ray diffraction (XRD, TD-3500, Dandong, China) using Cu Kα radiation operated at 35kV and 40mA; the scanning range 2θ was 10~80°; the scanning rate was 8°C/min; and the scanning speed was 2°/min. Raman spectroscopy measurements (Horiba LabRAM HR Evolution, HORIBA, Ltd., Japan) the degree of carbon residue with a laser wavelength of 405nm and a testing range of 50~4000cm^{-1}. EBSD measurements (TESCAN scanning electron microscope, TESCAN, Czech Republic) were performed using an

accelerating voltage of 20 kV, a sample tilt of 70°, and a hexagonal grid with a step size of 0.17 μm.

Table 2 The appropriate parameters of the UV curing process applied in this study

Parameters	Wavelength(nm)	Exposure time(s)	Power(mW/cm^2)	Layer Thickness(μm)
Value	385	20	200	30

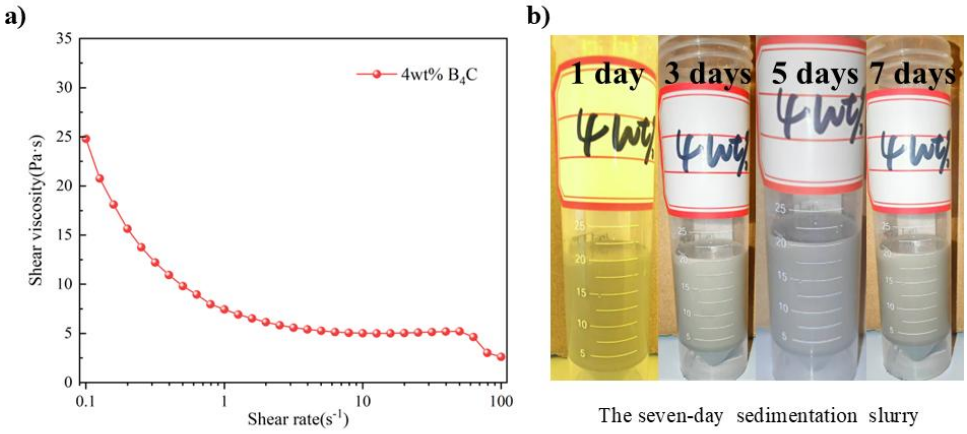


Figure 2. a) The rheology behavior of SiC suspensions with 4wt% B_4C sintering aids;b) The SiC slurry for the sedimentation test after 7days.

Table 3 Debinding and sintering experiment details

Sample	Debinding			Sintering		
	Temperature	Dwell time	Atmosphere	Temperature	Dwell time	Atmosphere
1#	450℃	4h	N_2	2150℃	2h	Ar
2#	500℃	4h	N_2	2150℃	2h	Ar
3#	550℃	4h	N_2	2150℃	2h	Ar
4#	600℃	4h	N_2	2150℃	2h	Ar
5#	650℃	4h	N_2	2150℃	2h	Ar

3 Results and discussion

3.1 Thermal decomposition and evolved-gas analysis during debinding

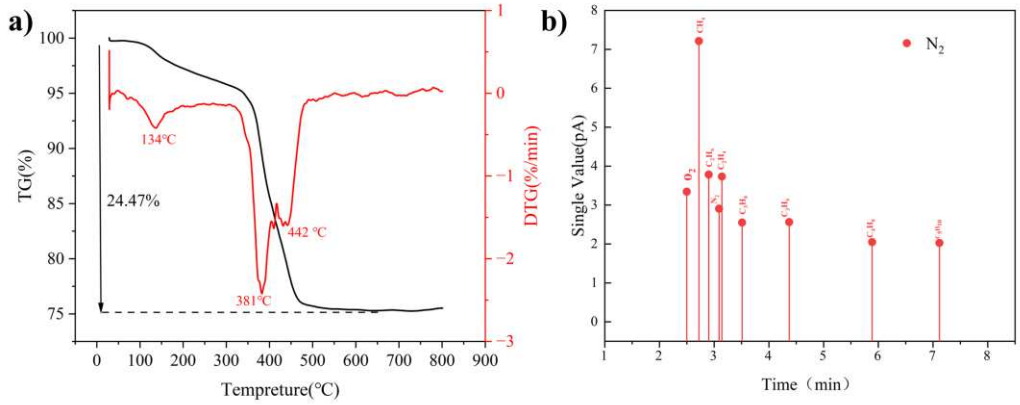


Figure 3. Thermal decomposition behavior of the green bodies during debinding: a) TG-DTG curves of the specimen; b) Gas chromatogram of the off-gas collected at 450 ℃

To clarify the decomposition behavior of the organic vehicle in the photopolymerized SiC ceramic green bodies during the debinding stage and to determine the final debinding temperature and the evolved products, thermogravimetric analysis (TG-DTG) was performed on the green bodies, and the debinding off-gas collected at 450 °C was analyzed by gas chromatography (GC), with the results shown in Figure 3. The photopolymerized green bodies were first heated under a protective atmosphere at a constant heating rate, during which the mass loss (TG) and the mass-loss rate (DTG) were recorded simultaneously as a function of temperature; in addition, the evolved gases were collected during the isothermal hold at 450 °C and, after separation by gas chromatography, the individual components were identified on the basis of retention time and quantified by peak area. The TG results show that the total mass loss of the green bodies was approximately 24.47%, and the mass-loss process can be divided into three stages: the mass loss below 134 °C corresponds to the removal of water and residual cleaning solvent; the slow mass loss occurring in the range of 134–380 °C originates from the thermal decomposition and volatilization of low-molecular-weight organic monomers; the most pronounced mass-loss peak appears in the range of 380–500 °C, with a DTG peak temperature of 442 °C, corresponding to the intense oxidative decomposition of the backbone polymer binder, after which the mass tends to be constant above 500 °C, indicating that the organic species have been

essentially completely removed. The GC results show that the main components of the 450 °C off-gas are CH_4, C_2H_6, C_2H_4, C_3H_8, C_4H_8 and a small amount of C_5H_{10}, i.e. low-carbon-chain alkanes and alkenes, among which the CH_4 peak exhibits the highest intensity, indicating that polymer cracking at this temperature proceeds predominantly via chain scission to form small-molecule hydrocarbons. Taken together, the debinding products of the present system can be classified into three categories: gaseous products, which consist mainly of the low-carbon-chain hydrocarbons identified by GC together with the carrier gas and are carried away by the flowing atmosphere; oily products, which condense as liquid residues and account for the mass loss that is not detected in the gas phase; and carbon black products, which remain in the matrix as residual carbon. Combining Figure 3, it can be seen that the region around 450 °C lies precisely within the intense decomposition range of the binder, where the mass-loss rate is high and the concentration of combustible hydrocarbons in the off-gas is elevated; therefore, the debinding schedule should adopt a slow heating rate and a prolonged isothermal hold in this range, so as to avoid cracking and blistering of the green bodies caused by the rapid release of gases. On this basis, the debinding temperature was further raised to and above the range of 450–650 °C in order to evaluate the influence of the final debinding temperature on the removal efficiency of organic species and to determine whether the binder can be completely decomposed and thoroughly removed within this temperature range.

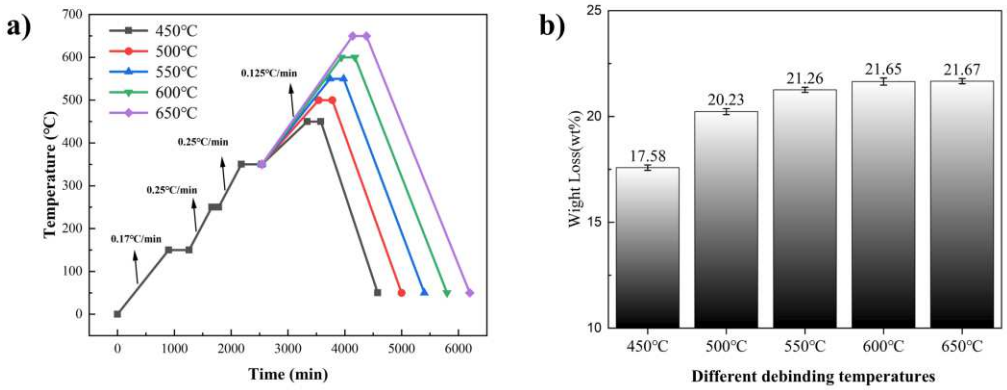


Figure 4. The debinding process and corresponding weight loss behavior: a) Different temperature-time profiles of the debinding process; b) Weight loss of SiC debinding samples at different debinding temperatures

Accordingly, the influence of the final debinding temperature on the evolution of residual carbon was further examined, and the degree of residual carbon defects under different debinding temperatures was characterized by Raman spectroscopy. For this

purpose, dwell times were incorporated at 150°C, 250°C, 350°C, 450°C, 550°C, 600°C and 650°C, with specific protocols outlined in Figure 4a: from 0°C to 150°C, heating rate = 0.17°C/min, held for 120 minutes; from 150°C to 250°C, heating rate = 0.25°C/min, held for 120 minutes; from 250°C to 350°C, heating rate = 0.25°C/min, held for 180 minutes and from 350°C to 450°C, heating rate = 0.125°C/min, held for 240 minutes. Subsequently, the samples were cooled freely to room temperature. The same sequence was performed but with higher temperatures for the final step at 450℃, 500°C, 550°C, 600°C and 650° C. The measured weight loss at different debinding temperatures is shown in Figure 4b. The weight loss reached 17.58 wt% at 450°C, increased to 20.23 wt% at 500°C, 21.26 wt% at 550°C, 21.65 wt% at 600°C, and finally stabilized at 21.67 wt% at 650°C. These weight-loss characteristics are governed by the staged pyrolysis behavior of the organic vehicle, which is described as follows：

The pyrolysis of the resin proceeds through several temperature-dependent stages, each of which controls the volatile release and the integrity of the evolving carbon network [25]. Below 300 °C, chain scission of the polymer releases small volatiles such as H_2O and CO_2; the associated mass loss is limited, but this stage marks the onset of microvoid formation within the matrix. In the range of 300–430 °C, binder degradation intensifies markedly, as reflected by the pronounced mass-loss rate and the corresponding endothermic DSC peaks [26]. This stage corresponds to the decomposition of the epoxy acrylate functional groups, and when the released gas is not removed at a sufficient rate it may accumulate locally and initiate cracks. Above this range, progressive dehydrogenation and radical recombination convert the fused-ring intermediates into polycyclic aromatic hydrocarbons [27, 28]. These reactions yield a structurally heterogeneous and polydisperse carbon network. The relative rates of volatile release and bond recombination thus control the composition of the debinding products: a high release rate favours the gaseous and oily fractions, whereas recombination retains part of the carbon in the matrix as carbon black. The measured weight loss reflects this competition, increasing rapidly from 17.58 wt% at 450 °C to 21.26 wt% at 550 °C and then changing only marginally, to 21.65 wt% at 600 °C and 21.67 wt% at 650 °C. The plateau above 600 °C shows that the gaseous and oily products have been essentially exhausted, and that further heating no longer removes material but instead continues to reorganize the residual carbon through dehydrogenation and aromatization. In this temperature range the residual carbon is therefore no longer a product of incomplete pyrolysis but a network whose degree of disorder is set by the extent of aromatization, which in turn determines its role in the

subsequent pressureless sintering.

To investigate the removal behavior of organic phases in photopolymerization ceramic green bodies at different debinding temperatures, EDS elemental mapping and quantitative analysis were performed on the raw powder and samples after debinding at 450–650 °C, with a focus on the evolution of the content and distribution of C and Si.

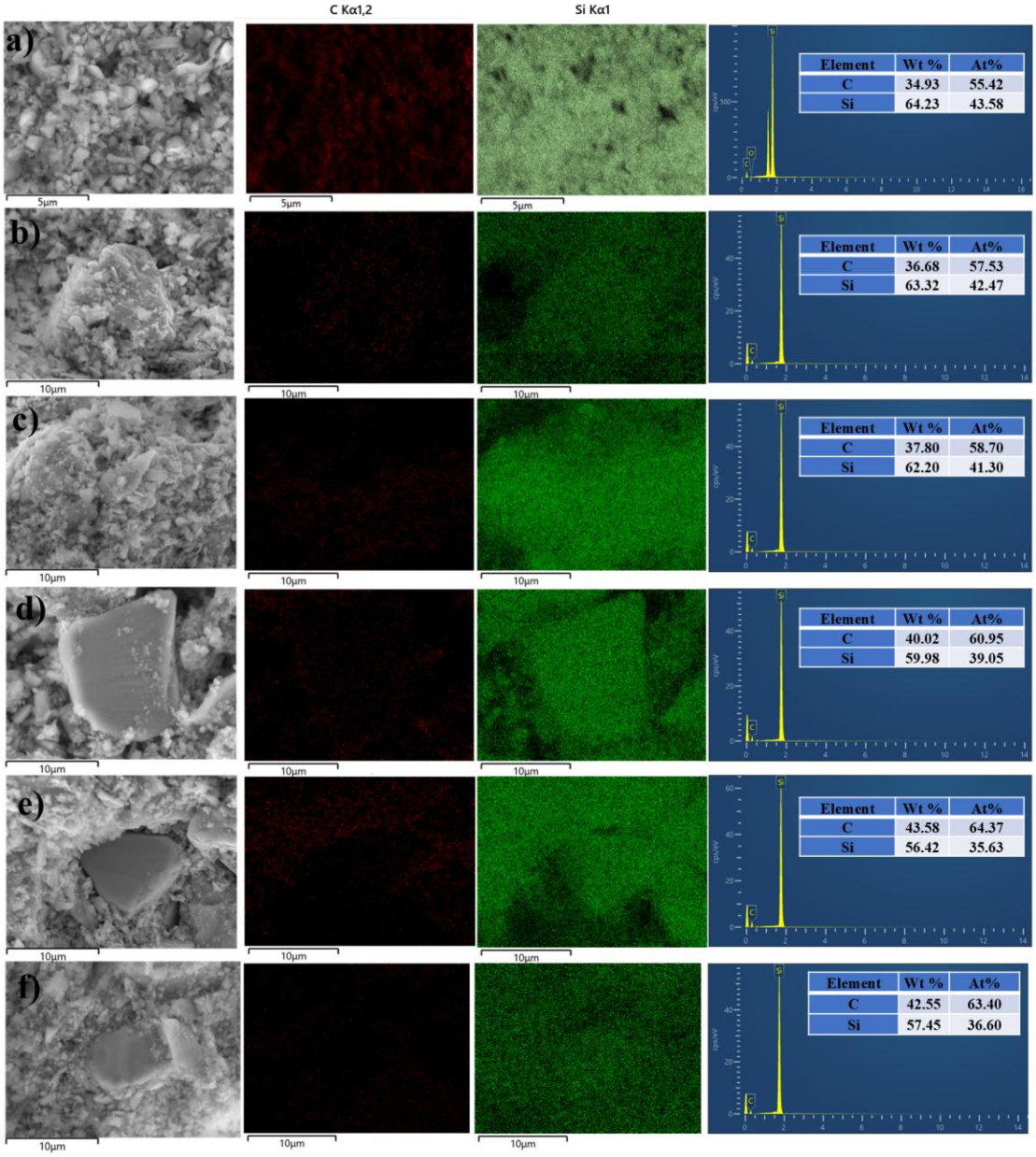


Figure 5. The SEM morphology and EDS elemental mapping of the raw powder and samples after debinding at different temperatures: (a)Raw powder; (b) 450 °C; (c) 500 °C; (d) 550 °C; (e) 600 °C; (f) 650 °C

As shown in Figure 5a, the raw powder exhibits C and Si atomic contents of 55.42 at% and 43.58 at%, which is mainly attributed to the powder synthesis process. As

shown in Figure 5b-f, with the debinding temperature increases from 450 °C to 650 °C, the relative mass fraction of C in the samples shows a continuously increasing trend: the C content is 57.53 at% in the sample at 450 °C, increases to 58.70 at% at 500 °C, rises to 60.95 at% at 550 °C, further increases to 64.37 at% at 600 °C, and reaches the highest value of 63.4 at% at 650 °C. Correspondingly, the Si content continuously decreases from 42.47 at% to 35.63 at%. This phenomenon, wherein the relative content of C increases rather than decreases with rising debinding temperature, is caused by the generation and enrichment process of residual carbon. During the debinding process, the resin undergoes incomplete oxidation reactions, and the macromolecular chain segments are prone to thermal polycondensation reactions, forming a more stable amorphous residual carbon, which adheres to the surfaces of powder particles and the inner walls of pores. As the temperature increases, small-molecule organics are preferentially removed, while the residual carbon phase gradually becomes enriched in the system, manifesting as an enhanced signal intensity of C in EDS mapping. The carbon residue behavior during the debinding process revealed by the EDS results provides a core prerequisite for the subsequent evolution of the pore structure: at the low-temperature stage, a large amount of organic phase and initial residual carbon fill and block the pores, restricting the opening and connectivity of the pores; as the temperature increases, the organic phase is gradually removed, the residual carbon becomes progressively enriched and finally agglomerated, and only then can the pores be gradually opened, expanded, and interconnected. Subsequent Raman spectroscopy will further reveal the microstructural evolution of carbon, while mercury intrusion porosimetry will directly verify the process of pore opening and framework reconstruction.

3.2 Residual carbon evolution: carbon content and structural ordering

On the basis of EDS elemental characterization, Raman spectroscopy was further employed to investigate the microstructural evolution of residual carbon during thermal debinding. This reveals the pyrolysis, carbonization and structural rearrangement behavior of the photosensitive resin precursors. The Raman spectra of samples after debinding at 450–650 °C are presented in Figure 6a. In the acoustic spectrum of silicon carbide, peaks are observed between 100 cm^{-1} and 700 cm^{-1}, representing the first-order transverse acoustic (FTA) and longitudinal acoustic (FLA) modes. In the optical spectrum, peaks appear near 800 cm^{-1} and 1000 cm^{-1}, corresponding to the first-order transverse optical (FTO) and longitudinal optical (FLO) modes [29]. As shown in Figure 6a, two typical characteristic peaks located at approximately 1350 cm^{-1} (D band)

and 1580 cm^{-1} (G band) are clearly identified. The D band corresponds to disorder-induced vibrational modes originating from amorphous carbon and structural defects, while the G band is attributed to the in-plane symmetric stretching vibration of sp^2-hybridized carbon in graphitic domains, confirming that resin pyrolysis during debinding primarily yields amorphous residual carbon phases [30]. The intensity ratio of the D band to the G band ID/IG is a reliable indicator for evaluating the structural ordering degree of residual carbon. In this study, the measured ID/IG values at debinding temperatures of 450 °C, 500 °C, 550 °C, 600 °C and 650 °C are 0.80, 0.72, 0.67, 0.63 and 0.83, respectively, exhibiting a distinct non-monotonic evolutionary trend with increasing temperature.

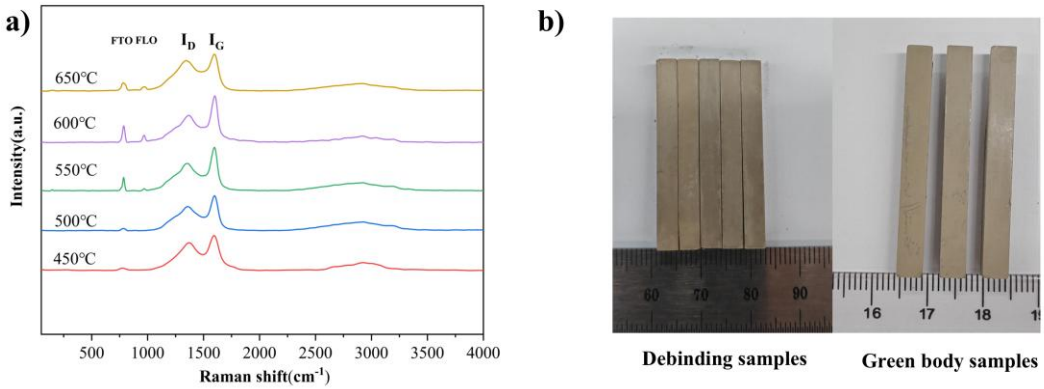


Figure 6. The influence of binder removal process on material structure and residual carbon: a) Influence of residual carbon on Raman spectroscopy features of SiC under different temperatures; b) Samples after debinding and before debinding (Temperature: 600 °C)

In the range of 450–600 °C, the ID/IG ratio continuously decreases from 0.80 to 0.63, demonstrating that the disordered amorphous carbon derived from resin pyrolysis undergoes gradual structural rearrangement. With rising debinding temperature, the proportion of ordered sp^2-hybridized graphitic carbon increases markedly, accompanied by a continuous reduction in structural defects and carbon disorder. This evolution corresponds to the thermal polycondensation and carbonization of resin macromolecular chains, in which metastable amorphous carbon is gradually transformed into thermodynamically stable structures [20], thereby reducing the defect density. Combined with macroscopic color variation of the samples as shown in Figure 6b, the visual transition from light gray to dark brown further intuitively verifies the continuous generation and progressive enrichment of residual carbon throughout the debinding process.

When the debinding temperature further increases to 650 °C, the ID/IG ratio

rebounds sharply from 0.63 to 0.83, indicating a remarkable increase in carbon structural disorder. This rebound is caused by severe thermal stress generated by intensive deep carbonization, which distorts and fractures the preformed ordered graphite-like carbon skeleton. Meanwhile, substantial newly formed amorphous defective carbon is continuously produced, and the excessive residual carbon undergoes long-range diffusion and local segregation enrichment. The synergistic effect of structural skeleton damage, new defect carbon generation and local carbon agglomeration collectively leads to the significant deterioration of carbon ordering for the consequent rebound of the ID/IG value[31].

By integrating EDS and Raman spectroscopic data, we identify a three-stage evolutionary mechanism that describes the behavior of residual carbon throughout the thermal debinding process. With increasing temperature, the pyrolysis and carbonization of the photosensitive resin are progressively intensified, and organic components are continuously converted into solid, fixed residual carbon, resulting in a sustained increase in the relative carbon content detected by EDS. At the optimal temperature of 600 °C, residual carbon undergoes effective thermal polycondensation and aromatization rearrangement, achieving the highest structural ordering and homogeneous distribution. In contrast, treatment at 650 °C triggers structural degradation and local segregation of residual carbon, inevitably increasing microstructural defects.

3.3 Pore architecture of the debound green bodies

Table 4: The data of pore structure and densification characteristic parameters by mercury intrusion porosimetry

Parameters	Debinding				
	450	500	550	600	650
Total Intrusion Vol. (mL/g)	0.14	0.16	0.18	0.18	0.19
Total Pore Area (m^2/g)	9.07	5.34	2.73	2.67	2.95
Packing Density (g/cm^3)	1.89	1.94	1.92	1.91	1.90
Porosity (%)	27.25	31.53	34.83	35.92	35.58
Tortuosity	3.94	3.5	3.05	3.44	2.68
Percolation Fractal Dim.	2.73	2.85	3.00	3.00	3.00

3.3.1 Open porosity, pore-size distribution and pore morphology

The debinding temperature is a key factor governing the removal behavior of organic phases and the reconstruction of pore structure in photopolymerization ceramic green bodies [32]. As shown in Table 4 and Figure 7a, the debinding temperature increases from 450 °C to 650 °C, the total mercury intrusion volume gradually increases from

0.14 mL/g to 0.19 mL/g, and the open porosity continuously rises from 27.25% to 35.58%, exhibiting a monotonically increasing trend. This change indicates that during the heating process, the photosensitive resin and organic additives undergo gradual pyrolysis and volatilization, and the space originally occupied by organic matter is released and converted into effective open pores accessible to mercury intrusion, with the internal pore channel system of the green body being continuously opened, and the pore volume and porosity significantly increasing with the removal of organic phases.

As shown in Figure 7a, the total pore area shows a significant decreasing trend with increasing temperature, rapidly decreasing from 9.07 m^2/g at 450 °C to 2.95 m^2/g at 650 °C. These results indicate that the green body is predominantly composed of fine, tortuous, and high-specific-surface-area micropores and transitional pores of carbon and SiC. As the temperature increases, small-diameter pores continuously merge, expand, and interconnect; the number of narrow-necked and ink-bottle pores decreases, the pore channel structure develops towards a coarser and more open direction, and the pore size distribution tends to be more uniform overall.

Figure 7b displays the incremental intrusion pore size distribution curves of specimens treated at different debinding temperatures ranging from 450 °C to 650 °C. It exhibits a single sharp pore size peak located between 100–300 nm, which corresponds to the dominant pore channels formed after organic binder removal. At 450 °C, the peak appears at the smallest pore diameter with the broadest distribution width and obvious low-amplitude tailing at pore sizes larger than 500 nm, indicating poor pore homogeneity. With the increase of debinding temperature from 450 °C to 650 °C, the peak position slightly shifts toward larger pore diameters, the width of the pore distribution gradually narrows, and the large-pore tailing above 1000 nm is significantly suppressed. This trend shows that the pore diameter plateaus, suggesting the main organic phase has been almost completely removed and the pore structure undergoes thermal stabilization and structural relaxation[33].

Two features of these data are relevant for the use of the material as a porous ceramic. First, the pore-size peak between 100 and 300 nm places the debinding-derived network in the macropore range of the IUPAC classification (above 50 nm), with the mesopore range contributing only to the sub-population that is responsible for the high total pore area at 450 °C. Second, MIP measures only the open, mercury-accessible porosity, so the value of 35.92% obtained at 600 °C is a lower bound of the total porosity: closed pores and pores screened by narrower necks are not intruded. The total porosity can be obtained independently from the bulk density, $\varphi_{total} = 1-\rho_{bulk}/\rho_{SiC}$, and the two quantities

are compared in Section 3.4. Reporting the open fraction explicitly is essential for a porous material, because it is the open network, and not the total porosity, that controls permeability, accessible surface area and infiltration behaviour.

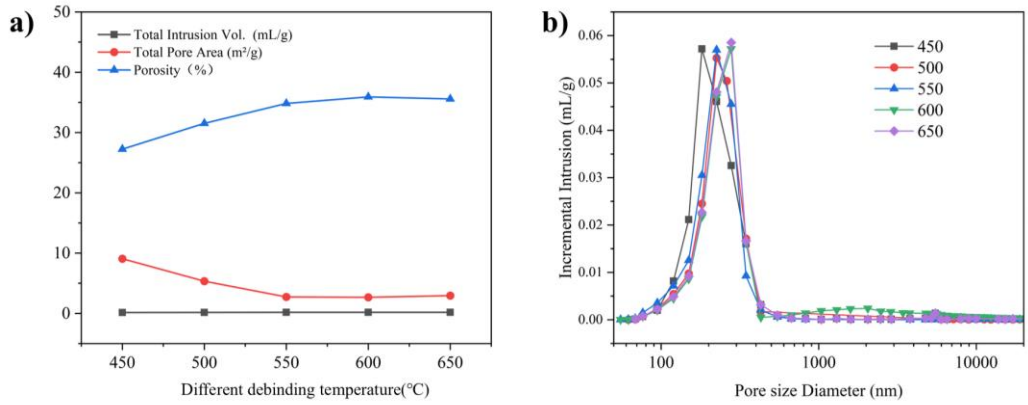


Figure 7. Pore structure characteristic parameters of SiC green body by mercury intrusion porosimetry at different debinding temperatures

3.3.2 Tortuosity, percolation and skeleton evolution

Tortuosity is a fundamental parameter that quantifies the degree of pore channel tortuosity and governs gas transport resistance within porous media [34]. In this study, as shown in Table 4, tortuosity continuously decreases from 3.94 at 450 °C to 2.68 at 650 °C, indicating that as debinding proceeds, the pore channels are continuously straightened and interconnected, the degree of path curvature decreases, and the gas escape resistance is significantly reduced. This facilitates the rapid escape of small-molecule gases during debinding and reduces the risk of blistering and cracking of the green body. The increase and subsequent stabilization of the percolation fractal dimension indicate that the pores within the green body gradually evolve from a dispersed and isolated state into a continuously interconnected three-dimensional pore network, with an effective percolation network being established around 550 °C. Thereafter, as the temperature continues to rise, the overall structure of the pore network no longer undergoes significant changes; it only optimizes and adjusts pore diameter and shape. The stable interconnection of the pore network provides structural assurance of thorough debinding and uniform shrinkage during the subsequent sintering process.

Considered together, the simultaneous decrease in tortuosity and the saturation of the percolation fractal dimension show that the debinding temperature changes the topology and not only the amount of the pore space. A network with a lower tortuosity and a fractal dimension close to 3.0 is geometrically closer to a space-filling, three-dimensionally connected structure, which increases the effective transport cross-section at a given porosity. For a porous material this is the relevant descriptor: two bodies of

identical open porosity can differ by a factor of about two in transport resistance when their tortuosity differs between 3.94 and 2.68, as it does between the samples debound at 450 °C and 650 °C. The same topological change explains why the pore-size distribution narrows while the total intrusion volume increases, since channels that merge and straighten convert small isolated and ink-bottle cavities into larger through-going channels.

The packing density increases from 1.89 g/cm³ to 1.91 g/cm³ at 600 °C and subsequently decreases slightly to 1.90 g/cm³ at 650 °C, as shown in Table 4. The continuous increase in packing density is attributed to the removal of a less dense carbon/organic residue compared to the SiC after the removal of organic phases, with an increase in contact points between particles and an improvement in the degree of skeleton densification. The slight change in packing density after 600 °C is not due to skeleton crack but rather to stress release and structural rearrangement of the particle system at high temperatures, which is a normal thermal relaxation behavior, indicating that the green body transitions from a dense and tense state to a thermodynamically stable state [35].

Based on the comprehensive analysis above, pore connectivity, and skeleton evolution reveals that the debinding process of photopolymerization ceramic green bodies in the 450–650 °C range unfolds via a clear and sequential mechanism: 1) as the resin continuously pyrolyzes, micropores are released, the pore area is large, the pore channels are tortuous, and the skeleton is gradually established; 2) the main organic phase is rapidly removed, the pore channels expand and interconnect; 3) the residual carbon is segregated, structural relaxation and rearrangement are completed. Overall, the pore channels of the green body are open, the network is interconnected, the skeleton is robust, and there is no crack or pore blockage. The debinding temperature influences microstructural evolution, yielding structurally stable, defect-limited green bodies for subsequent sintering densification. Among all tested conditions, 600 °C is identified as the optimal debinding temperature, where full decomposition of photosensitive resin yields disordered pyrolytic carbon. Post-debinding samples were subjected to high-temperature sintering. This evolution of carbon microstructure accounts for the pore evolution and skeleton reconstruction observed via mercury intrusion porosimetry, establishing an intrinsic linkage between debinding temperature, residual carbon morphology, and sintered pore features.

3.4 Porosity–strength relationship of the sintered porous SiC ceramics

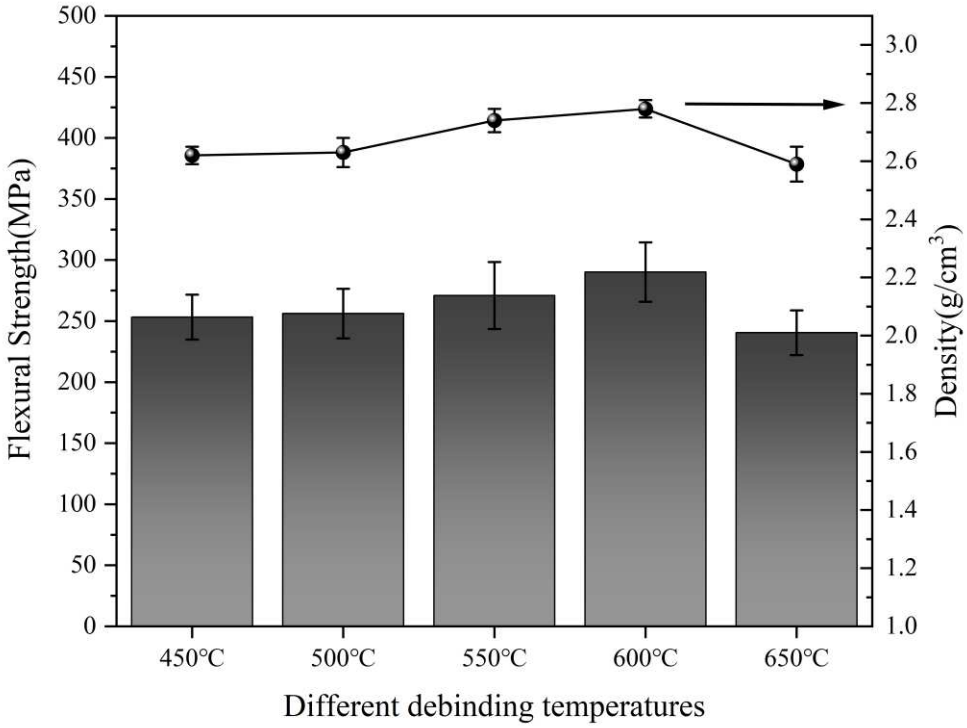


Figure 8. Flexural strength and sintered density of silicon carbide ceramics under different debinding temperatures.

The mechanical properties of SiC ceramics are significantly influenced by the type of additives, the microstructure and the porosity of the sample [36]. As described in Table 3, the samples were placed in a sintering furnace, heated to 2150 ° C, held at that temperature for 2 h and then allowed to cool naturally. After sintering, the mechanical properties were evaluated; each bending test was performed on a set of ten samples. Figure 8 shows bulk densities of 2.62 ± 0.03, 2.63 ± 0.05, 2.73 ± 0.02, 2.77 ± 0.03 and 2.59 ± 0.06 g cm^{-3} and the corresponding flexural strengths of 253.2 ± 18.4, 256.3 ± 20.5, 270.9 ± 27.4, 290.2 ± 24.3 and 240.5 ± 18.1 MPa for the ceramics debound at 450, 500, 550, 600 and 650 ° C. These densities correspond to 80.7 – 86.3% of the theoretical density of SiC, so the ceramics are deliberately porous rather than fully dense. This level of porosity is acceptable for lightweight structural and pore-function applications, and the strength is markedly higher than that of our previous VPP-fabricated SiC ceramics [17], although lower than that of dry-pressed SiC ceramics [37].

Expressed as relative values, the sintered densities correspond to 81.6%, 81.9%, 85.0%, 86.3% and 80.7% of the theoretical density of SiC (3.21 g cm^{-3}), that is, to total porosities of 18.4%, 18.1%, 15.0%, 13.7% and 19.3% for the samples debound at 450,

500, 550, 600 and 650 °C. For the optimal condition (600 °C) the value agrees with the area fraction of 13.99% obtained by image analysis of the SEM micrographs (Figure 11f) to within 0.3 percentage points, which supports the validity of the two-dimensional estimate and indicates that the residual pores are homogeneously distributed rather than concentrated in a few large defects. This sintered porosity (13.7–19.3%) is much lower than the open porosity of the corresponding green bodies (27.25–35.92%, Table 4); the difference is the pore fraction that is closed during solid-state sintering, and it amounts to about 22 percentage points at 600 °C against about 9 percentage points at 450 °C. The pore architecture established during debinding is therefore not lost on sintering but is partly retained, which is the basis for using the debinding temperature to set the final porosity.

The lower strength of the present specimens relative to dry-pressed SiC ceramics has its origin in the forming route rather than in the sintering chemistry. Dry pressing consolidates the powder under an external pressure, so that the green body reaches a high packing density with a uniform particle arrangement and contains no organic vehicle; the small pore population that survives sintering is evenly distributed [37]. In vat photopolymerization, the solid loading is limited to 55 vol% by the viscosity and curing requirements of the slurry, and about 45 vol% of the green body therefore consists of organic phase that has to be removed before sintering. The removal of this phase generates the open pore network of the green body, about 27.25-35.92%, as shown in Table 4, and pressureless solid-state sintering at 2150 °C closes only part of it.

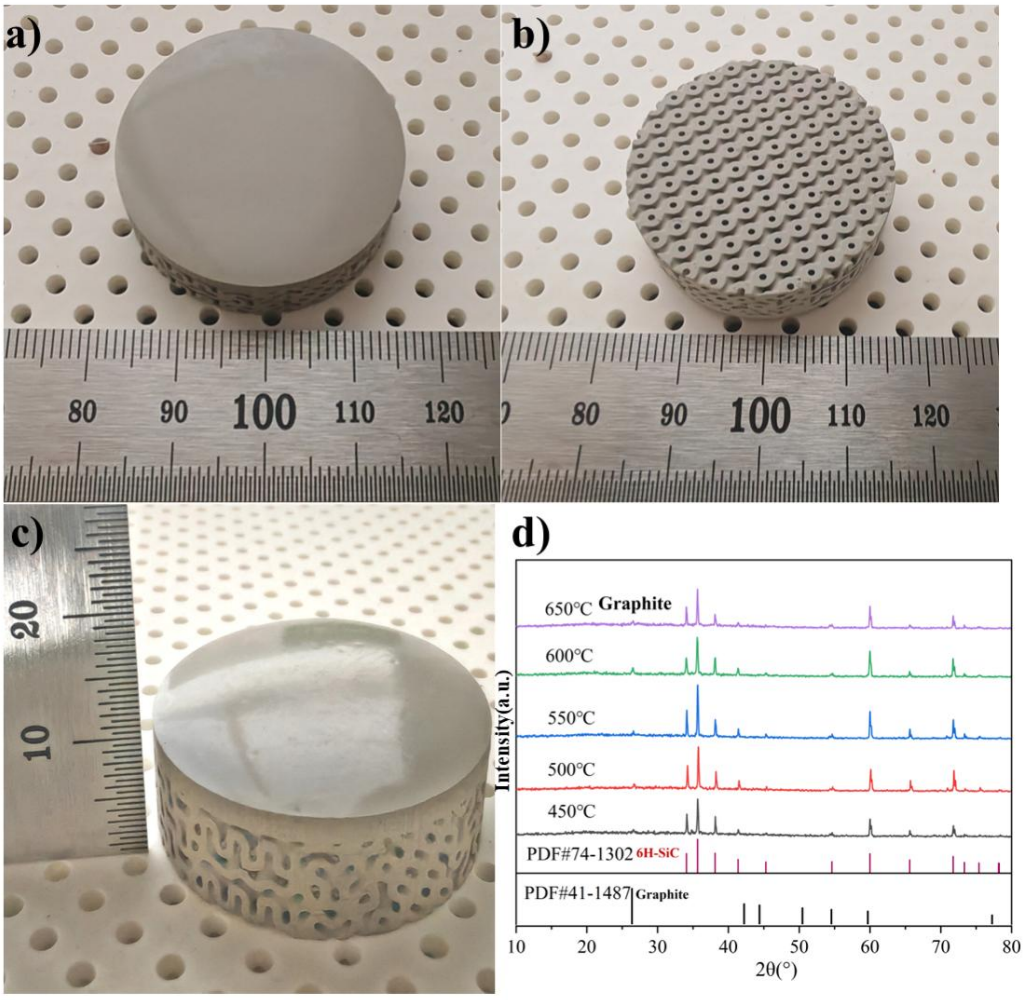


Figure 9. a)–c) as-printed SiC green bodies; d) XRD patterns of the ceramics debound at 450–650 °C and sintered at 2150 °C.

Figure 9a-c shows the green bodies of SiC fabricated from SiC slurry via 3D printing. Figure 9d compares the X-ray diffraction (XRD) patterns of the ceramics debound at 450-650 °C and sintered at 2150 °C. All five patterns are dominated by 6H-SiC, and the reflection at about 26.5° corresponds to the (002) plane of graphite, whose relative intensity is highest for the sample debound at 600 °C. Phase analysis therefore reveals coexisting graphite and 6H-SiC phases. This indicates not only the transformation of pyrolytic carbon into ordered graphite, but also that, although the defects associated with the residual carbon have been controlled, its content still requires strict regulation. The pore fraction described above is therefore the second variable that controls the mechanical properties. When the porosity does not exceed 25%, the relationship between porosity vp and strength σ can be approximated as follows [38]:

$$\sigma = \sigma_0 exp(-bv_p) \quad (4)$$

where σ is the strength of the porous ceramic body at a given porosity; σ_0 is the strength when the porosity is 0, v_p is the porosity; b is a constant related to the shape, orientation, and arrangement of the pores. It can be deduced that an increase in porosity decreases the strength, thereby reducing the strength of the samples. As the porosity increases, the contact area between the SiC grains decreases, which is conducive to the formation and propagation of microcracks and decreases the properties of ceramics. Therefore, increasing the contact area between powder particles can promote the shrinkage, crack, or closure of some pores driven by surface energy, thereby reducing pore defects and enhancing densification.

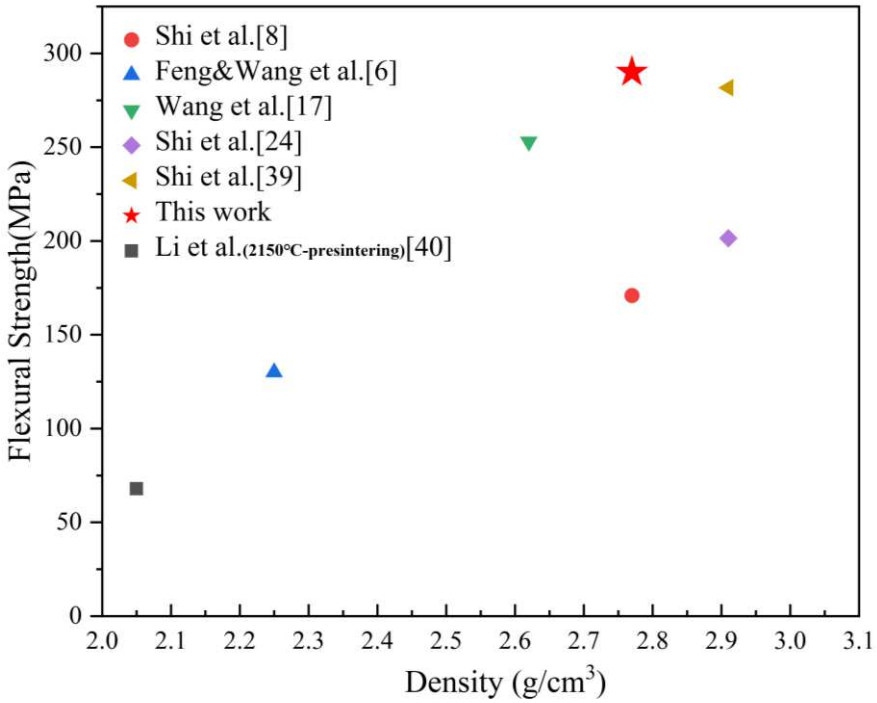


Figure 10. Comparative plots of flexural strength of pressureless SiC ceramics prepared by VPP processes [6, 8, 17, 24, 39, 40].

As shown in Figure 10, significant progress has been achieved in the fabrication of high-performance pressureless ceramics via VPP technology. The flexural strength of photocured SiC ceramics reaches 290.2 MPa. Such a mechanical property is superior to that of alumina-doped SiC ceramics with liquid-phase sintering additives[8], and remarkably higher than conventional zirconia ceramics [39]. The obtained material exhibits better performance among pressureless-sintered SiC ceramics fabricated via vat photopolymerization. The enhanced mechanical performance originates from the incorporation of B_4C and graphite composite solid sintering aids. Different from conventional liquid-phase sintering dominated by grain boundary glass phase formation, B_4C facilitates interfacial bonding and bulk densification via solid-state diffusion. This

strategy effectively restricts the generation of fragile grain boundary phases, endowing the sintered ceramics with superior mechanical strength and chemical stability.

3.5 Microstructure, grain-boundary graphite and pore aggregation

To reveal the microstructural correlations between debinding temperature, carbon residue behavior, and final sintering performance, SiC ceramics were subjected to microstructural and grain boundary phase distribution analyses, complemented by EBSD characterization to investigate the regulatory role of the residual carbon in sintering densification, grain growth, and grain boundary phase evolution.

The residual carbon evolution dictates the content and distribution of carbon residues in the green body. This, in turn, modulates the effectiveness of sintering aids during sintering, ultimately governing the densification degree, porosity, and mechanical properties of the final ceramics. Figure 11a-e shows the SiC ceramic samples after debinding at 450 °C, 500 °C, 550 °C, 600 °C, and 650 °C, respectively. The porosity was measured using ImageJ software, as shown in Figure 11f. The results indicate that the sample debinding at 600 °C has the lowest porosity, while the sample treated at 650 °C has the highest. The measured porosity values for debinding temperatures of 450 °C, 500 °C, 550 °C, 600 °C, and 650 °C are 18.90%±0.3%, 18.10%±0.5%, 15.04%±0.2%, 13.99%±0.3%, and 21.30%±0.6%, respectively. The microscopic mechanism underlying this difference requires further elucidation through microstructural characterization.

With $\sigma 0 = 394.9$ MPa, $b = 2.36$ and $R^2 = 0.949$, Equation (4) provides the quantitative link between the pore architecture established during debinding and the load-bearing capacity of the sintered body, and it defines the design space of the present material. Within the 13.7–19.3% porosity range the strength decreases by about 2.4% for each additional percentage point of porosity, which corresponds to the variation from 290.2 MPa at 13.7% to 240.5 MPa at 19.3%. The fitted b lies in the range typical of porous ceramics, and $\sigma 0$ approaches the strength of the corresponding dense solid. Because the phase composition is unchanged within the series (Figure 9d), the pore fraction is the dominant variable, and the scatter about the fitted line reflects the spatial distribution of the grain-boundary graphite discussed below rather than a change in the intrinsic strength of the solid phase. For a porous material the practical consequence is that the debinding temperature can be used as a single processing lever that sets the porosity and, through Equation (4), the strength.

First, from the SEM morphologies and porosity statistics of sintered samples subjected to different debinding temperatures (Figure 11a–f), it can be observed that the sample debinding at 600 °C exhibits smaller pore sizes, a more uniform pore

distribution, and more tightly bonded SiC grains. In contrast, the samples debinding at 450–500 °C show significantly increased residual pores, while the sample debinding at 650 °C displays local abnormal grain growth and pore aggregation. Combined with the previous EDS, Raman, and mercury intrusion porosimetry results, the following findings can be summarized:

When the samples are debinded at 450–500 °C, the organic phase is incompletely removed, leaving a substantial amount of disordered carbon remaining within the pore channels. This not only leads to pore blockage and low porosity during the debinding stage, but also hinders the contact between B_4C and SiC particles during sintering, thereby suppressing the solid-phase mass transfer process. Consequently, residual pores increase and densification decreases after sintering. When the sample is debinded at 600 °C, the organic phase is substantially removed, and the residual carbon exhibits the highest degree of ordering (ID/IG = 0.63). At this stage, the carbon is uniformly distributed in the form of a highly ordered graphite-like phase, which not only promotes the bonding between SiC grains as a sintering aid but also avoids local abnormal grain growth caused by the non-uniform distribution of disordered residual carbon.

When the debinding temperature increases to 650 °C, the photosensitive resin undergoes thorough and deep pyrolysis and carbonization, as shown in Figure 6a. A large number of pyrolytic carbon precursors undergo long-range diffusion and local segregation and enrichment. The excessively high heat treatment temperature disrupts the uniformly distributed ordered graphite-like carbon structure formed at 600 °C, while simultaneously generating a large amount of newly formed amorphous pyrolytic carbon and structurally defective carbon. This results in a rebound in the overall disorder degree of the residual carbon, which is fully consistent with the microstructural observation of significantly increased porosity in the sample sintered at 650 °C.

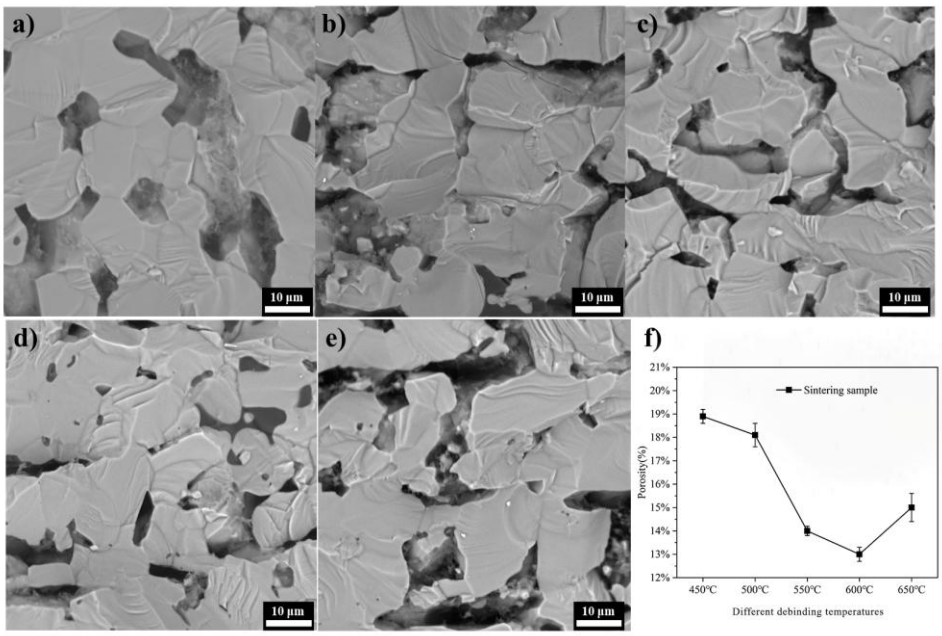


Figure 11. Sintered SiC ceramics derived from different debinding temperatures: a) 450 °C; b) 500 °C; c) 550 °C; d) 600 °C; e) 650 °C; f) porosity of SiC ceramic samples as a function of debinding temperature ranging from 450 °C to 650 °C.

Chen et al. demonstrated that the degree of structural ordering of the carbon source is a critical parameter influencing the sintering behavior of SiC ceramics [41]. Nevertheless, in the field of photopolymerization-based additive manufacturing, we can tailor the defect concentration of residual carbon by adjusting the debinding process, so as to facilitate sintering densification. To further investigate the distribution of carbon residues at grain boundaries and their influence on grain growth, this study employed the EBSD technique to analyze the grain boundary phase and crystallographic orientation of the sample debound at 600℃. Figure 12a shows an overlay of the EBSD grain boundary map and phase distribution map, revealing the presence of red-colored graphite crystals and green-colored 6H-SiC phase in the silicon carbide ceramic sample. The graphite in the sample comes from the transformation of residual carbon during high-temperature sintering, as well as from the carbothermal reduction of the sintering aid boron carbide. The phase distribution indicates that graphite crystals are mainly located along the grain boundaries of 6H-SiC, suggesting that graphite hinders normal grain growth. Meanwhile, the uneven distribution of graphite causes the formation of local texture along the 0001 direction, as shown in Figures 12b and c, indicating some degree of preferred orientation in this direction.

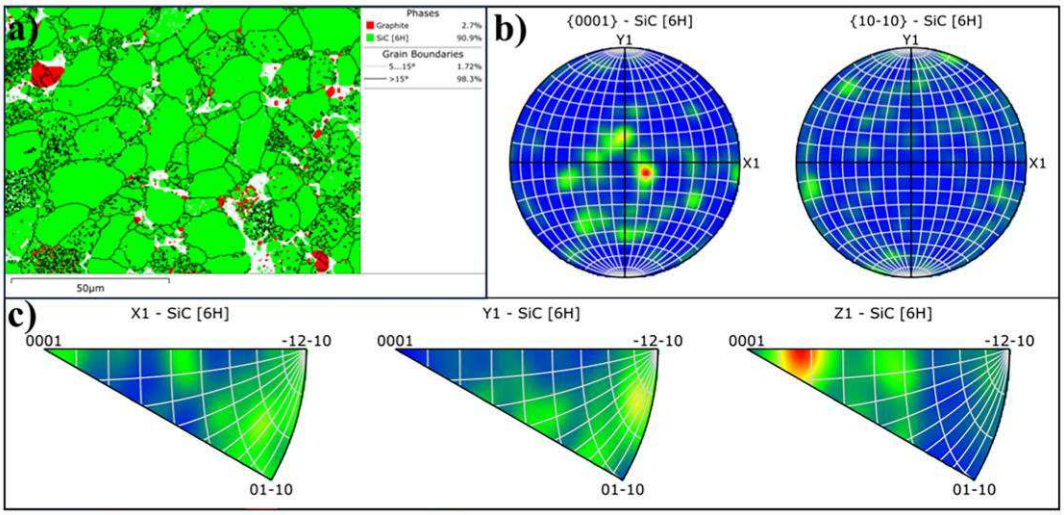


Figure 12. EBSD Analysis of SiC ceramic: a) phase identification map； b) Corresponding (0001) pole figure of the SiC layer showing crystallographic orientation. The X1 and Y1 axes in the figure correspond to the RD (normal to cross-section plane) and TD (tangent to particle surface within the plane) ; c) Inverse pole figure of the (0001) crystal plane

The microstructural differences induced by different debinding temperatures originate essentially from the differential evolution of residual carbon content, existing morphology, and spatial distribution. As shown in Figure 13, the graphite is disordered and insufficiently distributed, which cannot adequately eliminate the surface oxide layer, resulting in high grain boundary diffusion resistance and limited sintering mass transfer. Consequently, the number of micropores inside the final green body increases, and the densification degree remains low. Under the different debinding conditions, deep carbonization of the resin induces long-range diffusion and local segregation of residual carbon, leading to excessive accumulation of the graphite phase at grain boundaries. This weakens the interfacial bonding between particles, thereby triggering uneven grain growth, lattice distortion, and pore aggregation, which significantly deteriorate the sintering performance. Therefore, only an appropriate amount of uniformly distributed, highly ordered residual carbon at grain boundaries can effectively reduce the grain boundary energy, accelerate solid-state mass transfer, and achieve efficient solid-state densification without the formation of low-melting-point glassy phases.

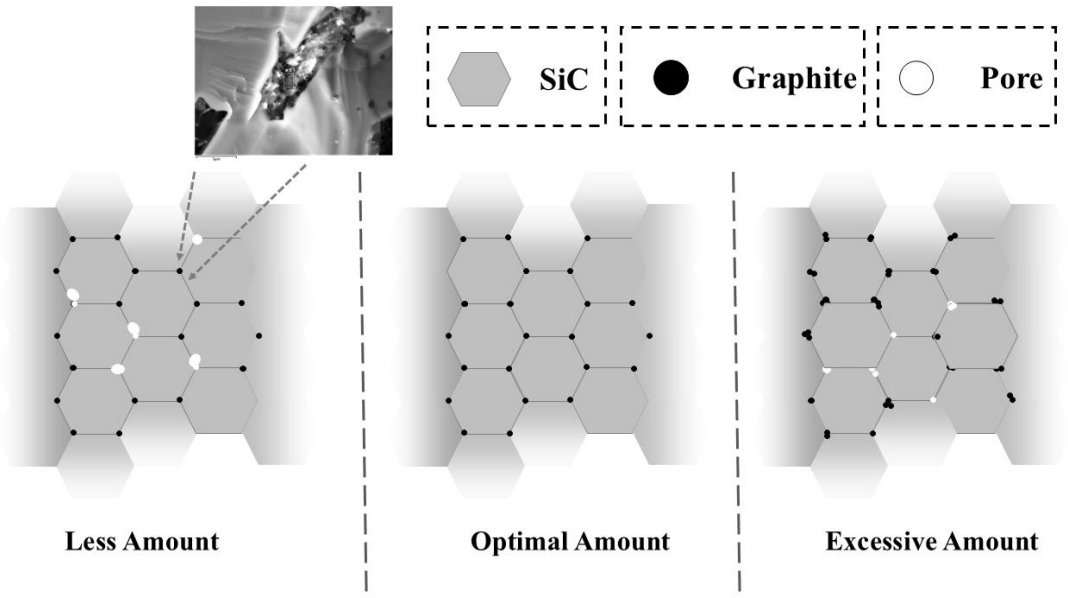


Figure 13. Schematic diagram of the effect of the graphite amount on porosity in SiC ceramic materials

When combined with macroscopic phase analysis by XRD, EBSD forms an effective complementary verification approach. The EBSD micro-area results also confirmed that the graphite phase continuously distributed along grain boundaries was the key to suppressing grain coarsening and optimizing microstructural uniformity. However, due to its limited depth of detection, EBSD can only reflect the characteristics of the surface micro-area, whereas XRD can provide the overall average phase information of the material. Therefore, the sample exhibits no macroscopic preferred orientation, showing only slight orientation differences in localized regions due to non-uniform residual carbon distribution. In summary, the residual carbon evolution behavior of SiC green bodies during the debinding process is the core key to regulating sintering densification, microstructural uniformity, and final mechanical properties.

4. Conclusions

This study introduces an effective method for producing high-performance silicon carbide ceramics with complex shapes through vat photopolymerization-based additive manufacturing. Although processing SiC ceramics has traditionally been difficult due to their high hardness and brittleness, we successfully manufactured SiC ceramics by carefully controlling the debinding temperature. This approach eliminates the need for complex molds typical of traditional machining methods.

The debinding temperature at 600 ℃ promoted a higher degree of ordering in the residual carbon structure, as indicated by a lower ID/IG ratio of 0.63. At this

temperature the green body also combined the highest open porosity (35.92%), compared with 27.25% at 450 ℃. As a result, the final SiC ceramic exhibited a porosity of 13.99% (13.7% from the relative density), a sintered density of 2.77 ± 0.03 g cm^{-3}, and a flexural strength of 290.2 ± 24.3 MPa, surpassing most reported VPP-fabricated SiC ceramics and comparable to certain liquid-phase sintered alumina materials.

From the perspective of porous materials, these results define a processing window in which the porosity of VPP SiC ceramics is set by the debinding temperature and the strength follows the Ryshkewitch–Duckworth relation, so that components can be designed either for maximum load-bearing capacity (13.7% porosity, 290 MPa) or for a higher accessible pore fraction (19.3% porosity, 240 MPa) without changing the slurry formulation or the sintering schedule. Because the open pore network is established before sintering, the same approach can be extended to graded or hierarchical pore architectures by locally varying the debinding schedule, which is not accessible to conventional pressing routes.

Authorship contribution statement

Zhiwei Wang: Methodology, Validation, Investigation, Visualization, Writing. Shijie Xu: Investigation. Li Yang: Investigation. Xiaomin He: Investigation. Jindan Tian: Supervision. Yanlin Jiang: Resources. Bohang Xing: Supervision. Paul Bowen: Supervision. Zhe Zhao: Conceptualization, Supervision, Funding acquisition, Reviewing.

Declaration of Competing Interest

The authors declare that they have no known competing financial interests or personal relationships that could have appeared to influence the work reported in this paper.

Acknowledgments

We gratefully thank the financial support by National Key Research and Development Project (No.2021YFB3701500), Shanghai Technical Service Center for Advanced Ceramics Structure Design and Precision Manufacturing (NO. 20DZ2294000), the Key Research and Development Projects in Zhejiang Province (No. 2022C01186) and the Leading Entrepreneurial Team Projects in Zhejiang Province (No.

2021R02016). Also, Prof. Paul Bowen (EPFL) for fruitful discussion under the consultant contract with CeramPlus.

References

1. Z. Zhao, X. Li, Y. Zhang, C. He, X. Zhang, H. Liu, and Q. Yan, Int. J. Appl. Ceram. Technol. 17, 1713–1722 (2020).

2. H. Zhang, Y. Yang, K. Hu, B. Liu, M. Liu, and Z. Huang, Addit. Manuf. 34, 101199 (2020).

3. S. Song, X. Lin, X. Ming, D. Lu, M. Sun, B. Wang, C. Bao, B. Lu, and E. Ma, J. Eur. Ceram. Soc. 45, 116970 (2025).

4. P. Li, J. Li, Q. Feng, T. Jin, Y. Bu, C. Wang, K. Luo, S. Ning, B. Xu, and Y. Zhu, Sci. Adv. 11, eadr4648 (2025).

5. S. Prochazka and R. M. Scanlan, J. Am. Ceram. Soc. 58, 72 (1975).

6. M. Feng, Z. Wang, W. Wang, J. Tian, Y. Jiang, B. Xing, and Z. Zhao, J. Eur. Ceram. Soc. 43, 7296–7305 (2023).

7. F. Chen, K. Liu, H. Sun, Z. Shui, C. Liu, J. Chen, and Y. Shi, Ceram. Int. 44, 254–260 (2018).

8. Z.-A. Shi, J.-M. Wu, C. Mao, L.-X. Fu, S.-L. Yang, J.-X. Zhang, and Y.-S. Shi, J. Eur. Ceram. Soc. 45, 116933 (2025).

9. C. Li, G. Wang, M. Hao, S. Wang, H. Jiao, and Q. Li, J. Eur. Ceram. Soc. 45, 117714 (2025).

10. A. Boretti and S. Castelletto, J. Eur. Ceram. Soc. 44, 1351–1360 (2024).

11. D. C. Jana, G. Sundararajan, and K. Chattopadhyay, Metall. Mater. Trans. A 49, 5599–5606 (2018).

12. J.-A. Yeom, Y.-W. Kim, W. K. Jung, D.-I. Cheong, and E. S. Kang, J. Eur. Ceram. Soc. 43, 3941–3949 (2023).

13. S. Gustafsson, L. K. L. Falk, E. Lidén, and E. Carlström, Ceram. Int. 34, 1609–1615 (2008).

14. L. Jin, K. Zhang, T. Xu, T. Zeng, and S. Cheng, Ceram. Int. 44, 20992–20999 (2018).

15. M. Riva, A. Airoldi, A. M. Caporale, L. Cavalli, and M. De Stefano Fumo, Composites Part A 175, 107774 (2023).

16. W. Li, C. Cui, S. Li, G. Zhang, B. Jin, J. Bao, C. Guo, Y. Zhang, B. Liu, and G. Wang, Addit. Manuf. 85, 104160 (2024).

17. Z. Wang, W. Wang, J. Tian, Y. Jiang, B. Xing, H. Nian, and Z. Zhao, J. Eur. Ceram. Soc. 44, 7512–7522 (2024).

18. S. Yamada, N. Sakamoto, J. Tatami, and M. Iijima, Adv. Powder Technol. 35, 104663 (2024).

19. Y. Oh, M. Heo, Y. W. Kim, and H. S. Kim, J. Am. Ceram. Soc. 108 (2025).

20. H. Xu, R. Zhou, C. Peng, R. Wang, and X. Wang, Chem. Eng. J. 526, 171–183 (2025).

21. E. Yildirim, M. Yurtsever, E. Yilgör, I. Yilgör, and G. L. Wilkes, J. Polym. Sci. B Polym. Phys. 56, 182–192 (2017).

22. S. Zhou, G. Liu, C. Wang, Y. Zhang, C. Yan, and Y. Shi, Mater. Des. 238 (2024).

23. H. Dong, S. Qin, H. Xie, P. Liu, Z. Liu, and X. Yang, J. Eur. Ceram. Soc. 45, 117675 (2025).

24. Z.-A. Shi, J.-M. Wu, Z.-Q. Fang, C. Mao, L.-X. Fu, Q.-W. Wang, S.-L. Yang, J.-X. Zhang, and Y.-S. Shi, Addit. Manuf. 84 (2024).

25. J. A. Onwudili, N. Insura, and P. T. Williams, J. Anal. Appl. Pyrolysis 86, 293–303 (2009).

26. K. Wang, M. Qiu, C. Jiao, J. Gu, D. Xie, C. Wang, X. Tang, Z. Wei, and L. Shen, Ceram. Int. 46, 2438–2446 (2020).

27. I. Lewis, Carbon 18, 191–196 (1980).

28. D. W. McKee, Annu. Rev. Mater. Sci. 3, 195–231 (1973).

29. S. I. Nakashima, M. Higashihira, K. Maeda, and H. Tanaka, J. Am. Ceram. Soc. 86, 823–829 (2003).

30. V. Dodevski, M. C. Pagnacco, I. Radović, M. Rosić, B. Janković, M. Stojmenović, and V. V. Mitić, Mater. Chem. Phys. 245, 122768 (2020).

31. M. Sevilla and A. B. Fuertes, Carbon 44, 468–474 (2006).

32. H. Li, Y. Liu, Y. Liu, Q. Zeng, K. Hu, Z. Lu, and J. Liang, Mater. Charact. 168 (2020).

33. C. Yu, T. Li, X. Hu, M. Liu, Q. Huang, L. He, and Y. Song, Macromolecules 56, 4738–4747 (2023).

34. Z. Lotfizarei, A. Mostafapour, A. Barari, A. Jalili, and A. E. Patterson, Addit. Manuf. 61, 103335 (2023).

35. K. Zhu, Y. Li, D. J. Huan, H. Liu, Z. Y. Li, Y. Jin, and C. L. Zhu, Macromol. Rapid Commun. 45, 12 (2024).

36. J. Fan, Q. Li, F. Jin, K. Yang, Y. Qiu, X. Yue, J. Liang, and J. Li, Ceram. Int. 49, 40705–40715 (2023).

37. H. Wu, Y. Yan, G. Liu, X. Liu, Y. Zhu, Z. Huang, D. Jiang, and Y. Li, Int. J. Appl. Ceram. Technol. 12, 976–984 (2015).

38. D. Feng, Q. Ren, H. Ru, W. Wang, Y. Jiang, S. Ren, and C. Zhang, Ceram. Int. 45, 23984–23992 (2019).

39. Z.-A. Shi, J.-M. Wu, C. Mao, L.-X. Fu, R.-Z. Zhang, S.-L. Yang, J.-X. Zhang, and Y.-S. Shi, Ceram. Int. 50, 44457–44466 (2024).

40. Y. Zhang, W. Duan, X. Sun, S. Zhou, K. Zhang, S. Li, B. Liu, and G. Wang, Ceram. Int. 51, 9893–9903 (2025).

41. R. Chen, J. Xin, J. Zhan, S. Li, and A. Mao, Ceram. Int. 50, 43082–43088 (2024).